

Fuzzy Logic Classification of S-Band Polarimetric Radar Echoes to Identify Three-Body Scattering and Improve Data Quality

VIVEK N. MAHALE

*School of Meteorology, Advanced Radar Research Center, and Center for Analysis and Prediction of Storms,
University of Oklahoma, Norman, Oklahoma*

GUIFU ZHANG

School of Meteorology, and Advanced Radar Research Center, University of Oklahoma, Norman, Oklahoma

MING XUE

School of Meteorology, and Center for Analysis and Prediction of Storms, University of Oklahoma, Norman, Oklahoma

(Manuscript received 25 November 2013, in final form 13 May 2014)

ABSTRACT

The three-body scatter signature (TBSS) is a radar artifact that appears downrange from a high-radar-reflectivity core in a thunderstorm as a result of the presence of hailstones. It is useful to identify the TBSS artifact for quality control of radar data used in numerical weather prediction and quantitative precipitation estimation. Therefore, it is advantageous to develop a method to automatically identify TBSS in radar data for the above applications and to help identify hailstones within thunderstorms. In this study, a fuzzy logic classification algorithm for TBSS identification is developed. Polarimetric radar data collected by the experimental S-band Weather Surveillance Radar-1988 Doppler (WSR-88D) in Norman, Oklahoma (KOUN), are used to develop trapezoidal membership functions for the TBSS class of radar echo within a hydrometeor classification algorithm (HCA). Nearly 3000 radar gates are removed from 50 TBSSs to develop the membership functions from the data statistics. Five variables are investigated for the discrimination of the radar echo: 1) horizontal radar reflectivity factor Z_H , 2) differential reflectivity Z_{DR} , 3) copolar cross-correlation coefficient ρ_{hv} , 4) along-beam standard deviation of horizontal radar reflectivity factor $SD(Z_H)$, and 5) along-beam standard deviation of differential phase $SD(\Phi_{DP})$. These membership functions are added to an HCA to identify TBSSs. Testing is conducted on radar data collected by dual-polarization-upgraded operational WSR-88Ds from multiple severe-weather events, and results show that automatic identification of the TBSS through the enhanced HCA is feasible for operational use.

1. Introduction

The three-body scatter signature (TBSS) was a term coined by Zrnić (1987) to describe a region of radar reflectivity aligned radially downrange from a highly reflective echo core (Lemon 1998). The TBSS is attributed to non-Rayleigh (i.e., Mie or resonance) scattering from a region of large hydrometeors made up of spongy ice spheres with a sizeable effective water thickness (i.e., wet hail) (Zrnić 1987). The signature was known originally as

a “hail spike” and was documented first by the Joint Airport Weather Studies project on 24 June 1982 by data collected from the National Center for Atmospheric Research (NCAR) C- (~5 cm) and S-band (~10 cm) Doppler radars (Wilson and Reum 1986). Other terms used to describe this signature include “flare echo” (Wilson and Reum 1988) and three-body scatter spike (also given by the acronym TBSS; Lemon 1998). Throughout this paper, the signature will be referred to simply as a TBSS (for three-body scatter signature or three-body scatter spike).

Zrnić (1987) attributed TBSS to a three-step scattering process by the electromagnetic wave transmitted from and received by the radar: 1) scattering of electromagnetic field by large hydrometeors to the ground, 2) backscattering by

Corresponding author address: Vivek N. Mahale, School of Meteorology, University of Oklahoma, Ste. 5900, 120 David L. Boren Blvd., Norman, OK 73072-7307.
E-mail: vmahale@ou.edu

the ground to hydrometeors, and 3) scattering by hydrometeors back to the radar. Figure 1 is a schematic that depicts the path and associated geometry of the radar signal responsible for TBSS. Large hydrometeors are located at point C, at a distance R from the radar. The radar beam strikes the large hydrometeors, which causes scattering toward the ground. The scattered signal strikes the ground in a conical region under the storm, where some of the signal is reflected by the ground. This power strikes the hydrometeors again, and some of the power returns to the radar.

Thus, it is important to note that TBSS is strictly a radar artifact, and it does not represent the hydrometeor scattering at the apparent data location (Lemon 1998). Therefore, for quantitative use of radar data for meteorological applications, such as the assimilation of radar data in numerical weather prediction (NWP) models and quantitative precipitation estimation (QPE) from radar reflectivity, it is important to identify and remove all TBSSs from the radar data. Automatic identification would eliminate (or at least reduce) the time spent to manually identify TBSSs in radar data, using software such as the NCAR Solo-II radar data editing and visualization program (Oye et al. 1995).

TBSS has been observed extensively by S-band radars (e.g., Wilson and Reum 1986, 1988; Zrnić 1987; Lemon 1998; Hubbert and Bringi 2000; Lindley and Lemon 2007; Picca and Ryzhkov 2012). Wilson and Reum (1988) conducted the first in-depth observational study of TBSS by looking at several cases in Alabama and Colorado at multiple radar frequencies. Lemon (1998) and Lindley and Lemon (2007) exclusively focused on radar data collected by S-band Weather Surveillance Radar-1988 Doppler (WSR-88D). In the observations, Lemon (1998) found that the reflectivity core intensity had to exceed ~ 62 dBZ for a TBSS to be present. Within TBSSs, the radar reflectivity factors were < 20 dBZ. While previous studies found TBSSs extended radially outward from 4 to 30 km (e.g., Wilson and Reum 1988; Lemon 1998), Picca and Ryzhkov (2012) observed an unusual TBSS that extended radially outward 80 km at S band.

Operationally, TBSS has been associated with severe weather such as microbursts and large hail at the surface (e.g., Wilson and Reum 1988; Lemon 1998; Lindley and Lemon 2007; Picca and Ryzhkov 2012). Lemon (1998) concluded that hail at least 2.5 cm in diameter should be expected at the surface with signature-bearing storms at S band. Lemon (1998) found that TBSS usually preceded large hail (and often strong winds) by 10–30 min. However, Lemon (1998) only focused on severe storms in the Great Plains. Wilson and Reum (1988) investigated TBSS in storms located in Colorado and Alabama. It was found that TBSSs in Alabama were not associated with

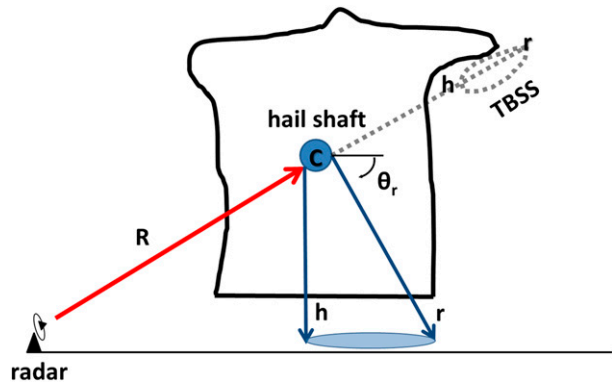


FIG. 1. Schematic of the radar signal path responsible for the TBSS. The blue circle at point C represents the hail shaft or high-reflectivity core. Also see section 2c for more details on the schematic. [Adapted from Wilson and Reum (1988).]

significant hail at the surface unlike in Colorado. It was assumed that the higher freezing level and higher-humidity environment reduce the probability of hail reaching the ground because of melting.

Polarimetric signatures associated with TBSS were investigated first by Hubbert and Bringi (2000). They found that measurements of differential reflectivity Z_{DR} within TBSS are very high close to the hail shaft, decrease, and then eventually become negative with range. It was also found that the copolar cross-correlation coefficient ρ_{hv} is typically 0.8 or less in a TBSS. Kumjian et al. (2010) defined the typical “polarimetric TBSS” as the beginning portion of the TBSS marked by high Z_{DR} and very low ρ_{hv} , located radially behind the reflectivity core. Using T-matrix calculations, Kumjian et al. (2010) was able to determine that the largest hailstones will not result in the typical polarimetric TBSS. As a result of Mie scattering and its effects on the scattering pattern of the hydrometeors, the Z_{DR} pattern does vary depending on the size of the hailstones and the wavelength of the radar.

Polarimetric radar measurements have been utilized in classifying radar echoes for different hydrometeors and nonmeteorological targets in hydrometeor classification algorithms (HCAs; Straka and Zrnić 1993). HCAs were first studied by Straka and Zrnić (1993) and have become more sophisticated in recent years (e.g., Zrnić and Ryzhkov 1999; Vivekanandan et al. 1999; Liu and Chandrasekar 2000; Zrnić et al. 2001; Lim et al. 2005; Park et al. 2009). Fuzzy logic has been the basis for a majority of HCAs (e.g., Liu and Chandrasekar 2000; Zrnić et al. 2001; Lim et al. 2005; Marzano et al. 2006; Park et al. 2009; Snyder et al. 2010). So far, no HCA identifies TBSS as a separate category.

The goal of this study is to utilize polarimetric radar measurements to automatically identify (i.e., classify) the radar echoes associated with TBSS, by enhancing an

existing HCA used at S band. The development of an enhanced HCA and the associated membership functions for the new TBSS class are outlined in section 2. The results of the enhanced HCA applied to polarimetric radar data for a number of independent cases are given in section 3. An overview of the results and some further discussion are given in the final section.

2. Development of the TBSS classification

a. Introduction of the modified HCA

Park et al. (2009, hereinafter P09) developed an HCA for polarimetric (S band) WSR-88D. The HCA is based upon fuzzy logic, and discriminates between 10 classes of radar echo: 1) ground clutter and anomalous propagation (GC/AP), 2) biological scatterers (BS), 3) dry aggregated snow (DS), 4) wet snow (WS), 5) crystals (CR), 6) graupel (GR), 7) big drops (BD), 8) light and moderate rain (RA), 9) heavy rain (HR), and 10) a mixture of rain and hail (RH). Their algorithm, or any other HCA that we are aware of, does not have the three-body scattering echo as an identified class.

In this study, a modified version of the P09 HCA is developed. This HCA is chosen because a version of it is implemented on the WSR-88D network. Three major simplifications are made to the original algorithm. First, specific differential phase K_{DP} is not used in the algorithm. In P09, K_{DP} (for radar reflectivity $Z < 40$ dBZ) is obtained from a slope of a least squares fit of heavily filtered differential phase Φ_{DP} (averaging of 25 successive samples). In this study, it was found that Φ_{DP} is incredibly chaotic and noisy within a TBSS. Therefore, the usefulness is already captured in the standard deviation of Φ_{DP} [$SD(\Phi_{DP})$], rather than in a calculation of K_{DP} for TBSSs. In all but three classes in P09, K_{DP} is already given zero weight. Second, there is no attenuation correction for the horizontal radar reflectivity factor Z_H or for Z_{DR} . As a result of the noisy Φ_{DP} , attenuation would be incorrectly calculated within TBSS. Third, confidence vectors are not used in the algorithm. The confidence vectors require information that is not included in the archived level-2 data such as the signal-to-noise ratio (SNR) and degree of beam blockage. Currently, all archived level-2 data are quality controlled to remove some low SNR. The modified P09 HCA provides a background of non-TBSS classes to test the new TBSS class. The results from our modified HCA are similar to those of the operational algorithm used to produce the HCA categories in the level-3 WSR-88D data.

Therefore, in our algorithm, the five variables utilized for the discrimination of hydrometeor types are 1) Z_H ; 2) Z_{DR} ; 3) ρ_{hv} ; 4) a texture parameter, $SD(Z_H)$; and

5) another texture parameter, $SD(\Phi_{DP})$. The texture fields are calculated for each gate by calculating the standard deviation along the radial using five gates (i.e., the current gate, and the two gates before and after the current gate along the radial). The standard deviations are calculated by dividing by the total number of observations n (i.e., 5) and not by $n - 1$.

Certain classes are restricted based upon the heights that bound the melting layer. P09 used the melting-layer detection algorithm developed at the National Severe Storms Laboratory. In this study, the depth of the melting layer is estimated using the ρ_{hv} rings. The top of the melting layer (i.e., the estimated freezing level) is the height associated with the farthest distance of the ρ_{hv} ring, while the bottom of the melting layer is the height associated with the closest distance of the ρ_{hv} ring. Above the freezing level, the only classes allowed are DS, CR, GR, and RH. Within the melting layer, the only class not allowed is BS. Below the melting layer, the only classes allowed are GC/AP, BS, BD, RA, HR, and RH.

All the membership functions, weights, and hard thresholds are the same as in P09. In P09 the membership functions are fitted to trapezoidal functions with a maximum value of 1 and a minimal value of 0. The trapezoidal functions are described by four parameters: x_1 , x_2 , x_3 , and x_4 . The weights, which are determined subjectively, characterize the discriminating efficiency of each variable with respect to each class.

For each radar gate, an aggregation value A_i for the i th class ($i = 1, 2, \dots, 10$) of radar echoes is calculated. As in P09, A_i is defined as

$$A_i = \frac{\sum_{j=1}^5 W_{ij} P^{(i)}(V_j)}{\sum_{j=1}^5 W_{ij}}, \quad (1)$$

where $P^{(i)}(V_j)$ is the trapezoidal membership function for the j th variable for the i th class and W_{ij} is a weight between 0 and 1 assigned to the i th class and j th variable. The classification of the radar echo is determined by which class has the largest aggregation value. The final step is a nine-point smoothing of the raw classifications to account for errors in the HCA output. In this smoothing technique, the mode of the raw classes of the current gate plus the surrounding eight gates (nine total gates) determines the smooth value of the current gate.

Figure 2 provides examples of classification results with the modified P09 HCA that does not have a TBSS classification. In the first example (Fig. 2a), the TBSS is

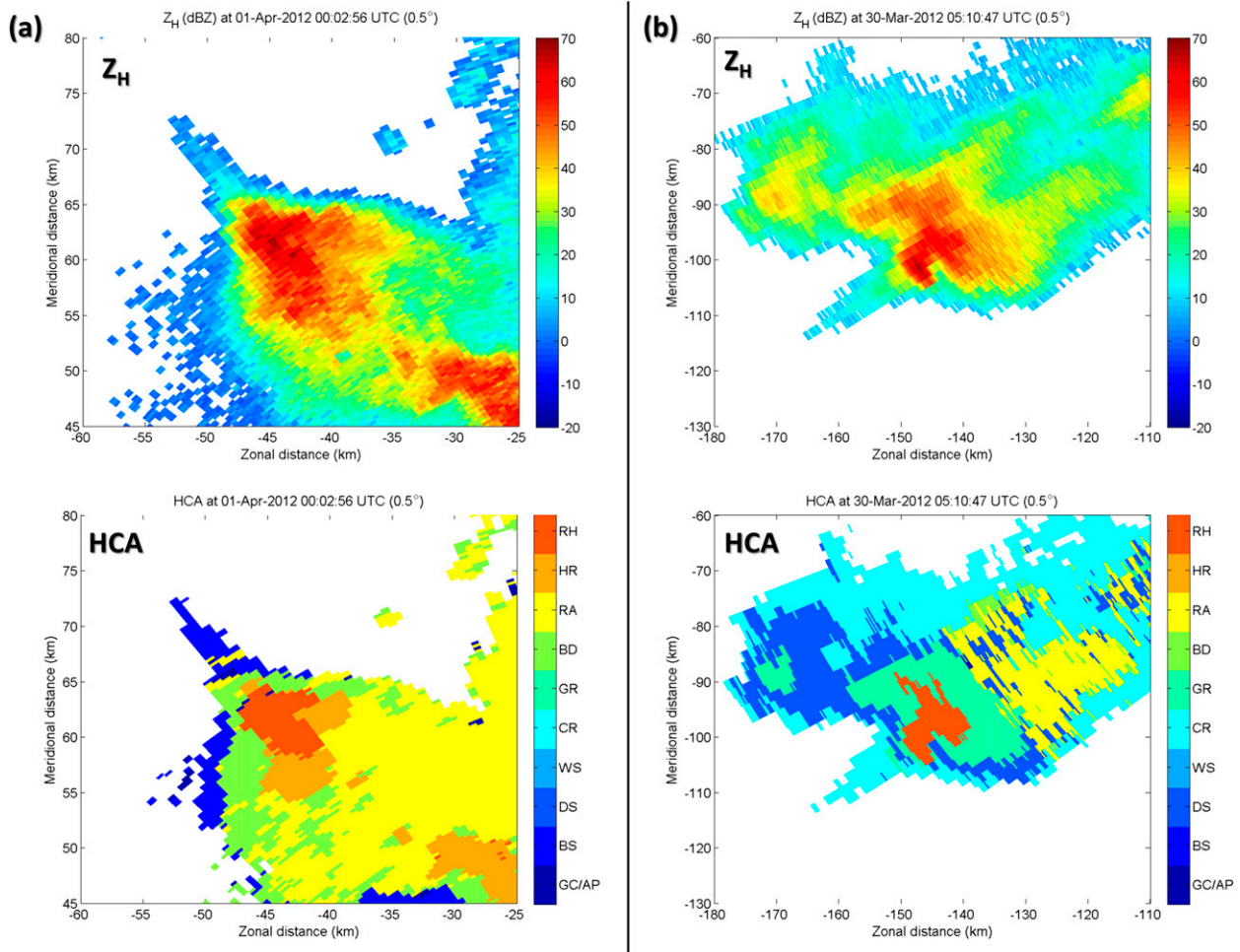


FIG. 2. Example events for which TBSS is (a) below the melting layer and (b) above the freezing level. Shown are (top) Z_H and (bottom) the hydrometeor classification. In both examples, no TBSS class is present in the hydrometeor classification algorithm. Therefore, the TBSSs are misclassified. The classifications in the bottom are 1) GC/AP, 2) BS, 3) DS, 4) WS, 5) CR, 6) GR, 7) BD, 8) RA, 9) HR, and 10) RH. Figures 8 and 9 show the two example events with the included TBSS classification.

below the melting layer. In this case, the TBSS is misclassified as primarily BS with some RA and GC/AP. In the second example (Fig. 2b), the TBSS is above the freezing level. As a result, the TBSS is misclassified primarily as CR with some GR. Similar misclassifications are present in WSR-88D level-3 HCA data (Fig. 3).

The next step is to add a new class of TBSS and develop a set of membership functions for the 11th class to create an enhanced HCA. Radar gates are subjectively identified as TBSS and are used as truth to determine the parameters for the enhanced HCA. Therefore, in this study, real radar observations of the TBSS are used to develop the membership functions for the TBSS class.

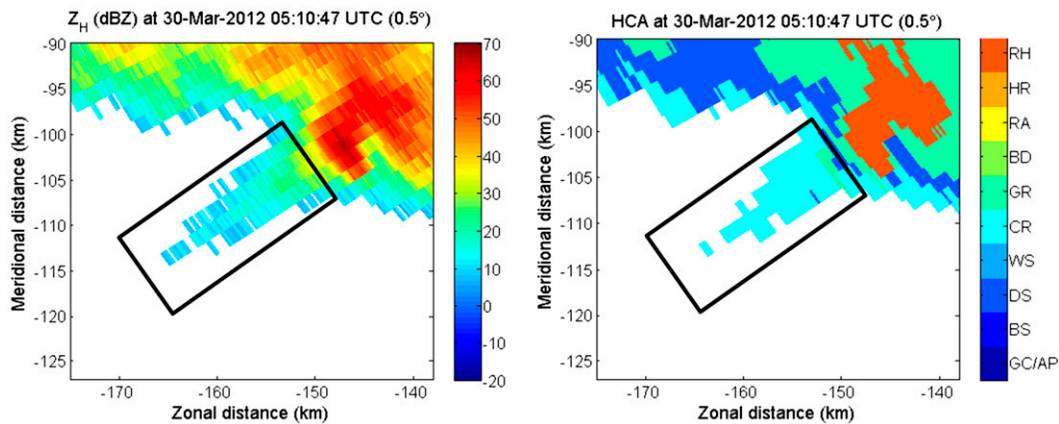
The following specific steps for developing the enhanced HCA that includes TBSS as the 11th category are taken. First, TBSSs are manually identified from radar data. All the values of the radar variables (i.e., Z_H , Z_{DR} ,

ρ_{hv} , Φ_{DP} , radial velocity, and spectrum width) are tabulated. Although velocity and spectrum width are not used in our HCA, statistics are still calculated for these data. The standard deviations of Z_H and Φ_{DP} are calculated at this stage as well. Second, analysis and probability statistics are conducted on the dataset to determine the best membership functions and weights. Third, any necessary constraints for the TBSS class are considered. Finally, the membership functions and weights are tested on independent radar data.

b. Data and statistics of radar variables in TBSSs

The experimental KOUN WSR-88D, located in Norman, Oklahoma, provided polarimetric radar observations for this study. Observations from the 14 June 2011 severe-weather event are used because of the large amount of TBSSs present in the dataset. KOUN is an S-band radar

(a) Level-2 (Modified HCA)



(b) Level-3

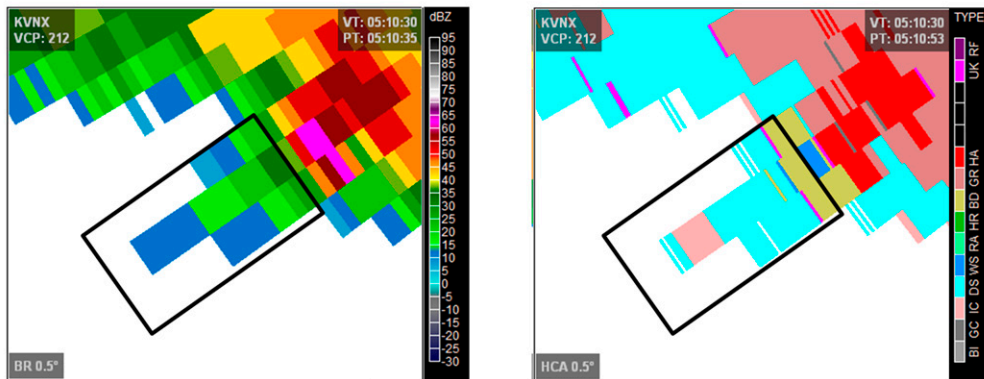


FIG. 3. Comparison of the (a) modified (level 2) HCA and (b) level-3 WSR-88D HCA on 30 Mar 2012 from KVNK. Values of Z_H are shown for both. The TBSS is boxed in black. The classifications are the same as in Fig. 2, but for the additions of unknown (UK) and range folding (RF) in the level-3 HCA. Both HCAs classify the TBSS as meteorological echoes. The modified (level 2) HCA misclassifies the TBSS as ice crystals (IC), DS, and GR. The level-3 WSR-88D HCA misclassifies the TBSS as IC, DS, WS, and BD. Note that the level-3 HCA is labeled HA instead of RH for rain-hail mixture and BI instead of BS for biological scatterers.

with a beamwidth of 0.925° , a range resolution of 250 m, and an azimuth increment of 0.5° for the lowest two elevations. At higher elevations, the azimuth increment is 1.0° . The effective beamwidth is 1.23° due to rotational smearing and its maximum unambiguous range is 230 km for radial velocity in a standard operating mode. KOUN was scanning with volume coverage pattern (VCP) 11, which is one of the primary VCPs used for severe convection (Office of the Federal Coordinator for Meteorological Services and Supporting Research 2013). In VCP 11, each scan volume takes approximately 5 min and includes 360° plan position indicator (PPI) scans collected at 0.5° -, 1.45° -, 2.4° -, 3.34° -, 4.3° -, 5.25° -, 6.19° -, 7.5° -, 8.69° -, 10.0° -, 12.0° -, 14.0° -, 16.7° -, and 19.5° -elevation angles.

Approximately 20 min of data between 2334 and 2356 UTC were analyzed for the presence of the TBSSs. These TBSSs were associated with one storm that was in

the process of splitting into two cells. After 0010 UTC, the storm produced hailstones up to 3.8 cm in diameter at the surface per the Storm Prediction Center (SPC) storm reports (SPC 2013). In total, 2975 radar gates of data were manually extracted from 50 different TBSSs. Note that TBSSs on different PPI scans were counted as separate TBSSs even if there was vertical or temporal continuity between the TBSSs. Within PPI scans, TBSSs were counted as separate TBSSs if there was an azimuthal break in the subjectively identified TBSS data. Velocity dealiasing and calculations of the texture parameter calculations were done on the dataset. These TBSSs were present at elevation angles ranging from 2.4° to 10.0° . All but two of the TBSSs were at least two radials wide azimuthally, while 11 were greater than five radials wide azimuthally. Additional TBSSs occurred after 2356 UTC, but 2975 radar gates of data were

TABLE 1. Summary statistics for 2975 radar gates from 50 TBSSs that were extracted from KOUN radar data collected between 2334 and 2356 UTC 14 Jun 2011.

	Z_H (dBZ)	Z_{DR} (dB)	ρ_{hv}	SD(Z_H) (dB)	SD(Φ_{DP}) (°)	Velocity ($m s^{-1}$)	Spectrum width ($m s^{-1}$)
Min	-5.5	-7.75	0.21	0.00	0.55	-39.5	0.0
Median	3.0	2.06	0.55	1.72	22.28	-14.5	6.5
Max	25.5	7.94	0.98	18.39	98.64	-1.5	17.5
Mean	3.95	2.32	0.53	2.13	26.11	-15.17	6.90
SD	5.18	3.47	0.18	1.63	15.51	6.20	2.07

deemed a large enough sample for the development of the membership functions.

Table 1 is a statistical summary for the radar variables extracted and/or calculated from the 50 TBSSs. Columns 1–5 describe the five variables that are used to develop membership functions for the TBSS class. Figures 4 and 5 are histograms that illustrate the distributions of all 2975 radar gates for the different variables.

The Z_H (Fig. 4a), SD(Z_H) (Fig. 4d), SD(Φ_{DP}) (Fig. 4e), and spectrum width (Fig. 5b) all have positively skewed distributions. The skewness is greatest on the SD(Z_H) distribution at ~ 3.2319 . This is followed by skewnesses of 1.2767, 0.8778, and 0.5284 for SD(Φ_{DP}), Z_H , and spectrum width, respectively. Visual inspections of the distributions validate these calculations. Recall that Lemon (1998) found that the TBSS has radar reflectivities < 20 dBZ. In this distribution, nearly all the radar gates are < 20 dBZ, except for a few gates. The generally higher spectrum width values also match the observations by Lemon (1998). Note that only 1 out of 2975 radar gates has a spectrum width that is $0 m s^{-1}$.

The Z_{DR} distribution (Fig. 4b) demonstrates a significant limitation of the level-2 radar data. The Z_{DR} is capped at 7.9375 dB. The reason behind this assertion is that 310 out of 2975 ($\sim 10\%$) gates have a value of exactly 7.9375 dB. It is statistically unlikely that 10% of the radar gates have this value because the precision of Z_{DR} is to four decimal points. The maximum Z_{DR} value was evident in all level-2 data from the cases in this study. If the radar data could provide greater Z_{DR} values, the distribution may have been normally distributed (i.e., a skewness near zero). There is a bias toward positive measurements for Z_{DR} (i.e., mean Z_{DR} of 2.32 dB and median of 2.06 dB). However, 27% of the Z_{DR} measurements are also negative.

Because of the difference in scattering patterns of the horizontally and vertically polarized waves, the bistatic Z_{DR} varies depending on the size of the hailstones. Figure 6 shows sample calculations of Z_{DR} as a function of scattering angle using Mie theory (Bohren and Huffman 1983) (TBSS mainly begins near 90°). As the hail size increases, the Z_{DR} becomes more chaotic as a function of

angle (Fig. 6). From experience in identifying TBSS in radar data, it is evident the majority of TBSSs start with positive Z_{DR} values, but there are some that start with negative Z_{DR} values and have a chaotic pattern. While it cannot be proven without observations at the height of the radar measurements, the theory would attribute these TBSSs to larger hailstones aloft.

A similar issue that affects the Z_{DR} distribution is present in the ρ_{hv} distribution (Fig. 4c). The minimum ρ_{hv} value in the level-2 radar data is 0.2083. In this case, 165 out of 2975 gates have a value of exactly 0.2083. As with the Z_{DR} , the minimum ρ_{hv} value was evident in all level-2 data from the cases in this study. If radar data could provide smaller ρ_{hv} values, the ρ_{hv} distribution may have been normally distributed.

The ρ_{hv} distribution matches previous observations by Hubbert and Bringi (2000) that 95% of the ρ_{hv} measurements are below 0.80. The low ρ_{hv} in the polarimetric TBSS can be explained by some previous nonpolarimetric observations by Lemon (1998). He (and through his personal communication with Zrnić) concluded that observations of broad spectrum widths in the TBSS indicated that measured velocities were not only from hail regions within the storm, but also from contamination by vegetation and other ground target motions. Natural land covers (such as trees, grass, and vegetation) have very low ρ_{hv} (Schuur et al. 2003). The low ρ_{hv} can be attributed to very irregular nonspherical shapes, which similarly explains the low ρ_{hv} in the tornado debris (e.g., Ryzhkov et al. 2005). Therefore, a decrease in ρ_{hv} is to be expected because of contamination by scattering from the ground.

The radial velocity distribution (Fig. 5a) has a skewness of -0.4716 , which indicates the distribution is slightly negatively skewed. It is noteworthy that out of 2975 radar gates, not a single gate has a positive or zero radial velocity measurement. The measured radial velocity associated with the TBSS has been shown to also have operational significance in determining the fall speed of TBSS-causing hydrometeors (Zrnić 1987; Wilson and Reum 1988). Wilson and Reum (1988) observed a TBSS where the velocities changed from initially all positive (maximum of $16 m s^{-1}$) to all negative

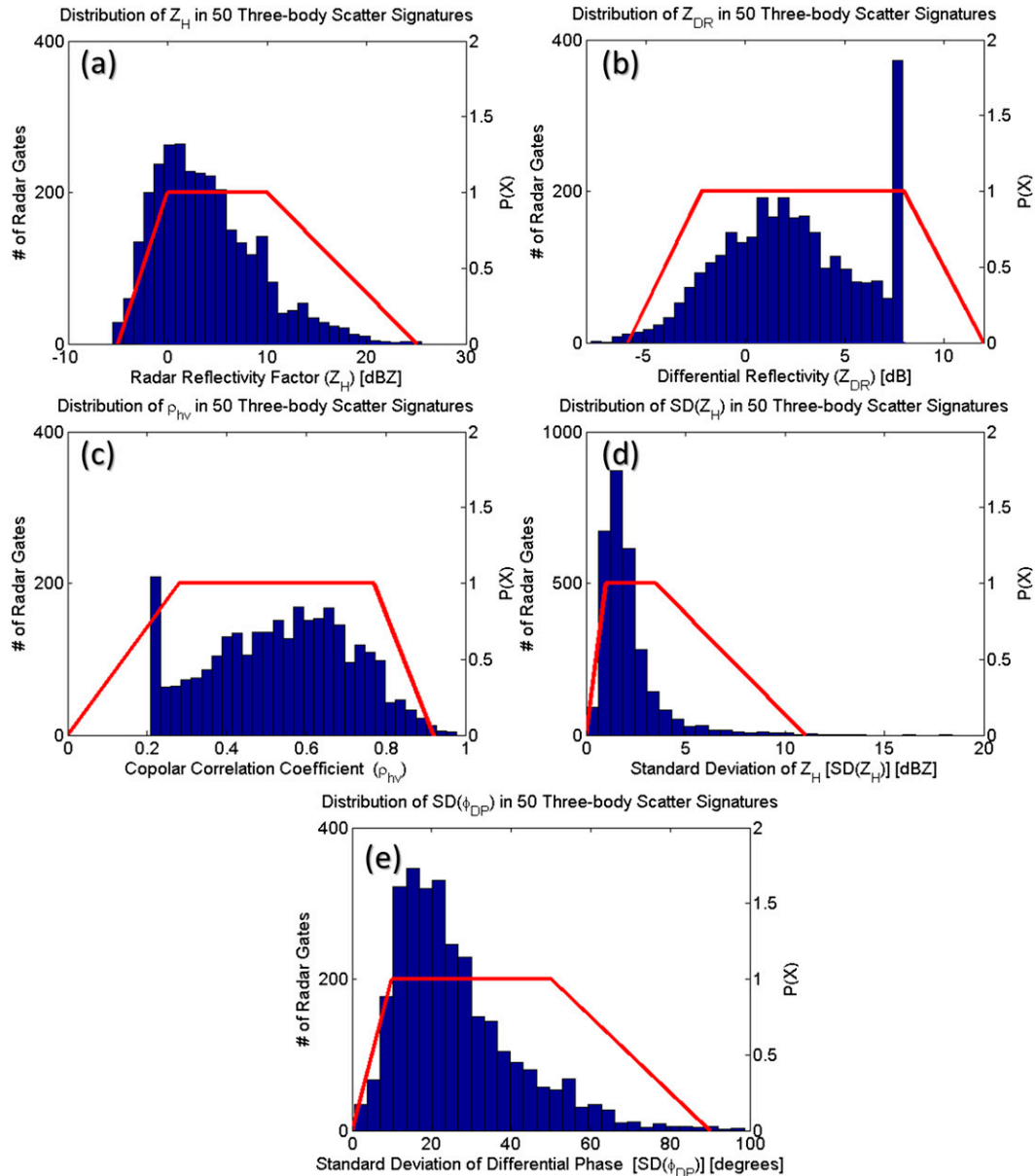


FIG. 4. The distributions of (a) Z_H , (b) Z_{DR} , (c) ρ_{hv} , (d) $SD(Z_H)$, and (e) $SD(\Phi_{DP})$ in 2975 radar gates from 50 TBSSs that were extracted from KOUN radar data collected between 2334 and 2356 UTC 14 Jun 2011. TBSSs on different PPI scans were counted as separate TBSSs even if there was vertical or temporal continuity between the TBSSs. The red lines are the derived trapezoidal membership functions.

(minimum of -20 m s^{-1}) in less than 8 min. During the same period, the core velocities changed from an average of $+4$ to -3 m s^{-1} . It was surmised that TBSS radial velocities evolved from positive to negative in response to an updraft changing to a downdraft. This was supported by an observation of a microburst shortly after the TBSS velocities became negative. However, Lemon (1998) had concerns about using TBSS velocities to detect microbursts. Lemon concluded that broad spectrum widths suggested that the velocities in the TBSS are from contributions of fall

speeds and radial speeds from a variety of hail regions, and from contamination by vegetation and other ground target motions. Also, since hailstones are responsible for three-body scattering, large terminal fall velocities are to be expected. Therefore, velocities are almost always negative, except within very strong updrafts (Lemon 1998). Therefore, the absence of positive radial velocity measurements is not surprising, as previous studies noted the rarity of positive radial velocity measurements in TBSSs (Wilson and Reum 1988; Lemon 1998).

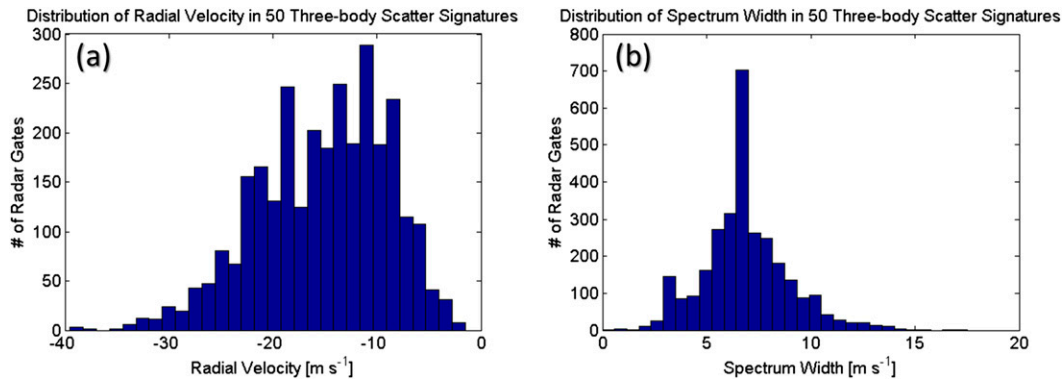


FIG. 5. As in Fig. 4, but for the distributions of (a) radial velocity and (b) spectrum width. No trapezoidal membership functions were derived for these two variables.

c. Determination of membership functions and hard thresholds

After subjectively analyzing the membership functions of P09, and taking into account the distributions for all the variables, the following criteria from the collected data are used to determine the four parameters in the five trapezoidal membership functions: x_1 , 0.5 percentile; x_2 , 20th percentile; x_3 , 80th percentile; and x_4 , 99.5th percentile.

As a result, 60% of the radar data collected would have a membership value of 1, and 39% of the radar data would have a membership value between 0 and 1. The remaining 1% of the radar data collected would have a membership value of 0. The minimum and maximum are excluded from the calculation of x_1 and x_4 , respectively, to account for outliers in the dataset. The physical origin of these outliers could be mixed targets and estimation errors in the radar variables. These parameters are also rounded to what is considered reasonable precision for each variable (e.g., ρ_{hv} rounded to the nearest hundredth). Note that these criteria can easily be modified if necessary.

These criteria are modified for the Z_{DR} and ρ_{hv} membership functions. As noted earlier, the maximum Z_{DR} in the level-2 radar data is 7.9375 dB, and the minimum ρ_{hv} is 0.2083. Theoretically, it is safe to assume that higher Z_{DR} and lower ρ_{hv} values would have been present. Therefore, if $x_4 = 8$ dB for the Z_{DR} membership function (i.e., 99.5th percentile), the membership value would be artificially too low (i.e., nearly zero) in the case where Z_{DR} was 7.9375 dB. A similar situation would be present if $x_1 = 0.21$ for the ρ_{hv} membership function. Assuming a Gaussian distribution and adding a buffer, the standard score calculation results in a Z_{DR} value of approximately 12 dB at the 99.5th percentile. As a result, the Z_{DR} membership function for the TBSS (i.e., x_4) is set to 12 dB instead of 8 dB. For the ρ_{hv} membership function, x_1 is set to 0.00 instead of 0.21 to account for the radar data's

limitation. Table 2 is a summary of the parameters for the membership functions for the TBSS class at S-band frequency. These parameters are overlaid on the distributions in Fig. 4.

Next, the weights for the different classes are determined. Recall the weights characterize the discriminating efficiency of each variable with respect to the class. P09 subjectively determined these weights. The weights in their scheme had values of 0, 0.2, 0.4, 0.6, 0.8, or 1.0. Each variable's weight was different for each of the 10 classes. For the TBSS membership functions, Z_{DR} and $SD(\Phi_{DP})$ have high membership values that encompass nearly the entire range of those variables. As a result, there is a high overlap between those trapezoidal functions and the trapezoidal

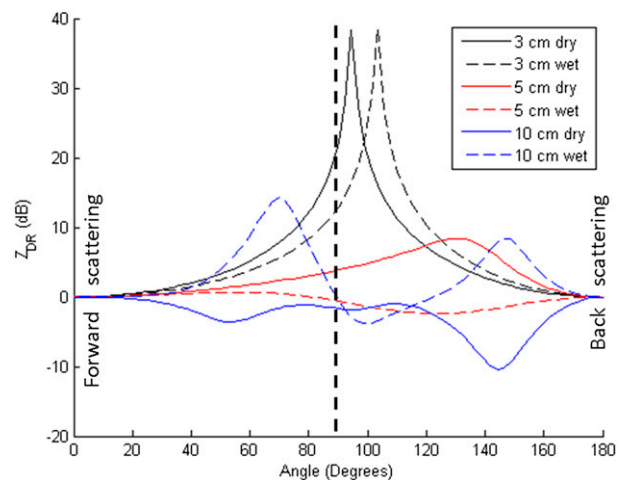


FIG. 6. Values of Z_{DR} as a function of angle for 3-, 5-, and 10-cm-diameter dry and wet spherical hailstones. These values were calculated using the Mie approximation assuming wavelength $\lambda = 10.7$ cm (S band). The dry hailstones were calculated with no fractional water content; the wet hailstones were calculated with 10% fractional water content. The dotted black line represents 90° (downscatter Z_{DR}).

TABLE 2. Parameters of the trapezoidal membership functions for the TBSS class at S-band frequency.

	$P[Z_H \text{ (dBZ)}]$	$P[Z_{DR} \text{ (dB)}]$	$P[\rho_{hv}]$	$P[\text{SD}(Z_H) \text{ (dB)}]$	$P[\text{SD}(\Phi_{DP}) \text{ (}^\circ\text{)}]$
x_1	-5	-5.9	0.00	0	0
x_2	0	-2.2	0.28	1.0	10
x_3	10	8.0	0.77	3.5	50
x_4	25	12.0	0.92	11	90
Wt	1.0	0.2	1.0	1.0	0.2

functions of other classes in the scheme of P09. This is not the case for the other three variables. Therefore, Z_{DR} and $\text{SD}(\Phi_{DP})$ must be weighted less than the other three variables. As a result, Z_{DR} and $\text{SD}(\Phi_{DP})$ are weighted at 0.2, while Z_H , ρ_{hv} , and $\text{SD}(Z_H)$ are weighted at 1.0. These weights can be modified if necessary.

Finally, any constraints to restrict the class are determined. P09 called these constraints “hard thresholds.” No restrictions are placed on the TBSS class based on the heights bounding the melting layer. Recall that a TBSS always occurs downrange from a highly reflective echo core (Lemon 1998). This is the crux of the scattering theory for the signature. Therefore, it seems reasonable (if not obligatory) to make a hard threshold based on this fundamental aspect of theory. As a result, a high-reflectivity core and RH classification must exist uprange from a possible TBSS classification. To be conservative, a threshold of 58 dBZ is used even though studies have suggested that reflectivity echo cores that result in a TBSS are associated with larger reflectivity values at S band (e.g., Lemon 1998). Examination of the geometry of the TBSS formed the basis of this hard threshold.

The scattering path’s angle of incidence with respect to the ground θ_r will determine the distance r that the signal will travel from point C to the ground (Fig. 1). The shortest path (i.e., the fastest time of arrival) will be for vertical paths directly below the large hydrometeors ($\theta_r = 90^\circ$), as noted by an h in Fig. 1. Therefore, the TBSS begins at distance h from point C. The length of the TBSS will depend on the maximum length of r since the signals travel a total distance of $2(R + r)$, and will be displayed as a radial distance $R + r$ from the radar.

Because the TBSS starts a distance h from the hail core, it is reasonable to assume that the maximum distance a TBSS may begin to appear downrange from a hail core is 10 km (the scale height of the troposphere). Applying this hard threshold is a two-step process. First, there is a check to see if there is at least one radar gate with a radar reflectivity ≥ 58 dBZ and at least one gate with RH classification, uprange 10 km (40 gates) from a possible TBSS class. If there is, then the TBSS class would be allowed for that gate. If there is not at least one radar gate 10 km uprange with a 58-dBZ measurement and at least

one radar gate with RH classification, a second check is conducted. In this check, if there is at least one TBSS class 2 km (eight gates) uprange, the TBSS class would be allowed for this gate. This check is implemented because of lengthy TBSSs; some of the distant radar gates would not pass the first check because the 58-dBZ core is >10 km away. Essentially, this check is looking for radial continuity. If this check fails, then the TBSS class is not allowed for that radar gate. The class with the next-highest aggregate value will replace the TBSS class.

One other hard threshold was considered, based upon a radar variable that was not used in the fuzzy logic portion of the HCA—radial velocity. Radial velocity was a variable used as a hard threshold in P09 HCA for the ground clutter and anomalous propagation class. They had a hard threshold that no ground clutter or anomalous propagation would be allowed if the radial velocity was $>1 \text{ m s}^{-1}$. Recall that no zero or positive radial velocity measurements are present in the distribution (Fig. 5b). Therefore, it was considered to include a constraint that no TBSS would be allowed if the radial velocity was $\geq 0 \text{ m s}^{-1}$; however, Wilson and Reum (1988) documented a TBSS that (briefly) had positive measured radial velocities in a strong updraft. In addition, all the TBSSs used to determine the parameters were from two storms that were generally moving toward or at an approximately constant range from the radar during the time frame of the extracted radar data. Zrnić (1987) determined that mean Doppler shifts associated with the TBSS are caused by both the vertical and true radial components of hydrometeor velocities. Because the storms were generally moving toward the radar, a negative bias in velocity would be expected from the radial component of the hydrometeor velocities. Therefore, a hard threshold using measured radial velocity is not utilized.

3. Analysis and results

The enhanced HCA is tested on five different significant hail events that occurred between 15 June 2011 and 22 April 2013. Table 3 is a summary of all the cases. These events are from five different operational WSR-88D that

TABLE 3. Summary of five significant hail events upon which the modified HCA was tested. Each of these events had a TBSS.

Date	PPI time (UTC)	Radar	Max Z		Hail time (UTC)	Max hail (cm)	Freezing level (km)	Melting level (km)
			Elev	Vol				
15 Jun 2011	0014	KOUN	63	72	0020	6.4	3.8	2.6
30 Mar 2012	0510	KVNX	67	68	0515	10.2	3.2	1.8
1 Apr 2012	0002	KBMX	68	71	0007	7.6	3.1	1.9
29 Mar 2013	2341	KTLX	69.5	72	2342	6.4	2.8	1.8
22 Apr 2013	2359	KICT	74	74	0004	5.1	2.9	1.8

had been upgraded to dual-polarization mode. All of these events had reported hailstones between 5.1- and 10.2-cm diameters at the surface. All of these events also had a TBSS aloft, as detected by radar. The hailstone reports are from the public storm reports that are aggregated by the SPC from the local National Weather Service (NWS) Weather Forecast Offices (WFOs) (SPC 2013). Therefore, it is possible that some event times and hail sizes are approximate; however, the radar data from these events suggests that all of the reports are reasonable.

In addition to the enhanced HCA classifications, radar reflectivity factor and ρ_{hv} are shown for each case study. These radar variables were picked because it is easiest to visually confirm the presence of a TBSS in these data. The quality-controlled radar reflectivity factor is also shown for each event. In the quality-controlled data, all non-meteorological targets (i.e., GC/AP, BS, and TBSS) are removed to demonstrate the benefits for NWP and QPE.

The enhanced HCA is also tested on the KOUN radar data that were collected on 15 June 2011. Note that these radar data are from immediately after the radar data that were used to develop the membership functions. This was done to prevent testing the membership functions on the same dataset that created the membership functions. In this event, a left-split storm produced a 6.4-cm-diameter hailstone at the surface at approximately 0020 UTC. Figure 7 is the radar scan from the 3.3°-elevation angle at 0014 UTC, 6 min before the hailstone was reported at the surface. At the 3.3°-elevation angle, the maximum radar reflectivity factor is 63 dBZ at ~2.2 km above radar level (ARL) (Fig. 7a). In several ≥ 60 -dBZ gates ρ_{hv} is < 0.80 , indicating the presence of hail mixed within the precipitation (Fig. 7b). In the entire volume scan, the maximum radar reflectivity factor was 72 dBZ at ~4.9 km ARL. The freezing level was ~3.8 km ARL, and the melting layer extended down to ~2.6 km ARL. Therefore, this TBSS at 3.3°-elevation angle extended into the melting layer.

In the HCA output (Fig. 7d), a few TBSS radar gates are misclassified as BS; however, for the quality-controlled radar reflectivity factor (Fig. 7c), this misclassification has no effect on the results because all nonmeteorological targets are removed. Even for real-time operational use,

the misclassification is not detrimental because it is clear when analyzing the HCA output that there is a TBSS downrange from a high-reflectivity core. Otherwise, there are no obvious false TBSS gates present in the HCA output for this storm.

The second event the enhanced HCA is tested on occurred on 30 March 2012. Radar data collected by the KVNX WSR-88D near Enid, Oklahoma, are used to test the enhanced HCA for this hail event. In this event, a nocturnal supercell produced a 10.2-cm-diameter hailstone at the surface at approximately 0515 UTC. Figure 8 is an example that shows the time evolution of a developing TBSS from 0442 to 0456 UTC. Without the added capabilities of dual-polarized radar measurements, the TBSS is not apparent until much later radar scans in radar reflectivity. The area of TBSS remained fairly constant for the next two radar scans, until 0510 UTC. Figure 9 is the radar scan from the 0.5°-elevation angle at 0510 UTC, 5 min before the hailstone was reported at the surface. A TBSS is now evident in reflectivity. At the 0.5°-elevation angle, the maximum radar reflectivity factor is 67 dBZ at ~3.6 km ARL (Fig. 9a). The ρ_{hv} within the 67-dBZ core is between 0.81 and 0.86, indicating the presence of hail (Fig. 9b). In the entire volume scan, the maximum radar reflectivity factor was 68 dBZ at ~7.4 km ARL. The freezing level was ~3.2 km ARL, and the melting layer extended down to ~1.8 km ARL. Therefore, this TBSS at 0.5°-elevation angle was above the freezing level.

In the HCA output (Fig. 9d), there is a slight discontinuity in the TBSS classification. The HCA output has TBSS class followed downrange by CR or GR class and then TBSS class once again. There is a very sharp gradient in ρ_{hv} where the HCA transitions from GR to TBSS classification. The sharp cutoff of reflectivity in the quality-controlled radar reflectivity factor (Fig. 9c) and the downrange change of class to CR or GR suggest the algorithm may have slightly overclassified the TBSS. A more gradual reflectivity gradient is more realistic, as seen by the reflectivity gradients elsewhere in the precipitation data. A downrange change from precipitation to TBSS to precipitation within the same storm is not realistic either. Therefore, it is reasonable to assume

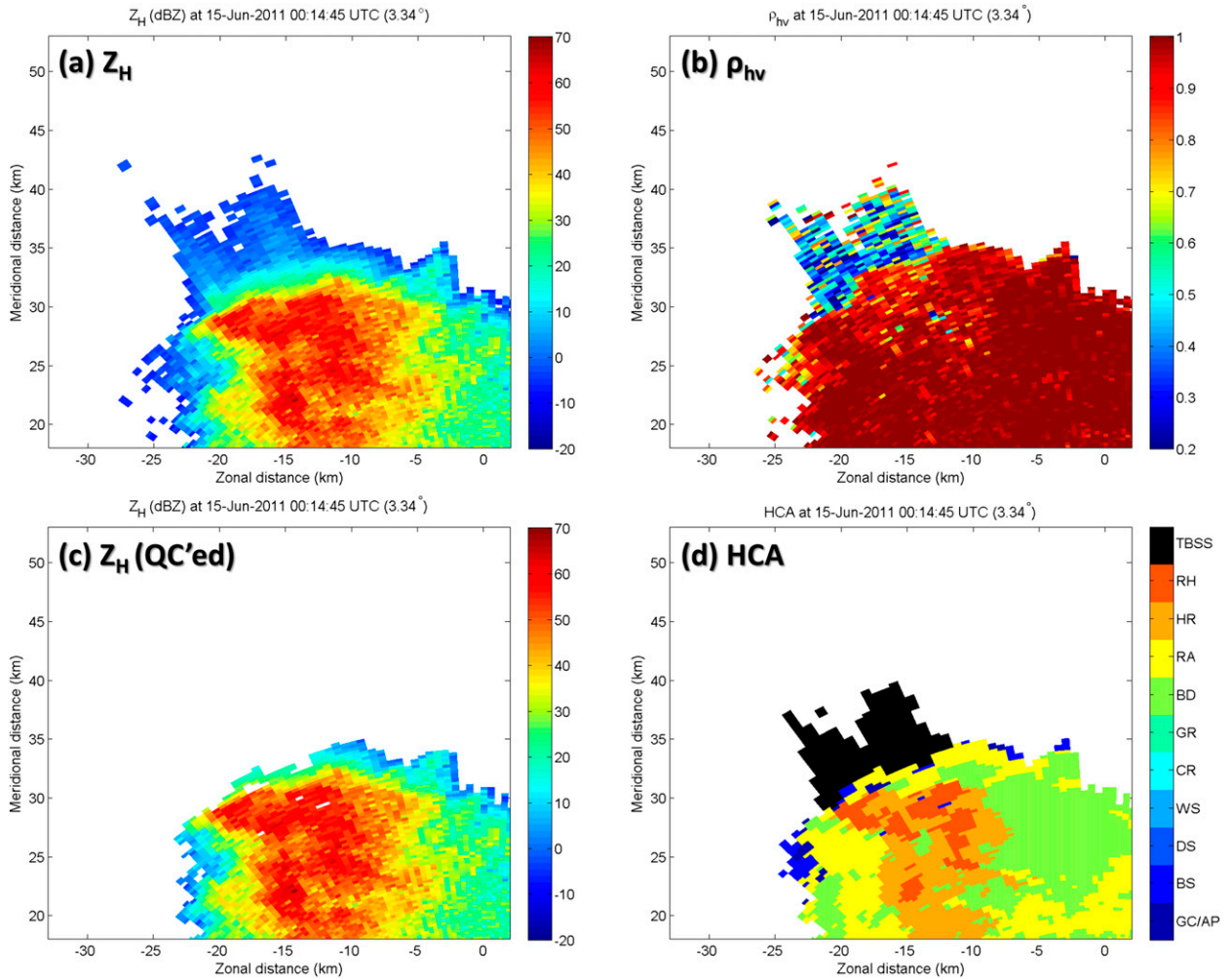


FIG. 7. Example event on 15 Jun 2011 from KOUN associated with 6.4-cm hail at the surface. Shown are (a) Z_H , (b) ρ_{hv} , (c) quality-controlled Z_H (removes GC/AP, BS, and TBSS), and (d) enhanced hydrometeor classification. In (d), the classifications are 1) GC/AP, 2) BS, 3) DS, 4) WS, 5) CR, 6) GR, 7) BD, 8) RA, 9) HR, 10) RH, and 11) TBSS. Axes are labeled relative to KOUN.

there is a mix of radar returns from both the TBSS artifact and the hydrometeors in some of the radar gates. Otherwise, the results for the classification of the TBSS seem very good in this case.

The third event the enhanced HCA is tested on occurred the next day on 1 April 2012. Radar data collected by the KBMX WSR-88D near Birmingham, Alabama, are used to test the HCA for this event. In this event, an evening supercell produced a 7.6-cm-diameter hailstone at the surface at approximately 0007 UTC. Figure 10 shows the radar scan from the 0.5° -elevation angle at 0002 UTC, 5 min before the hailstone was reported at the surface. At the 0.5° -elevation angle, the maximum radar reflectivity factor is 68 dBZ at ~ 1.1 km ARL (Fig. 10a). The ρ_{hv} within the 67-dBZ core is 0.94; however, some of the ≥ 60 -dBZ gates have ρ_{hv} as low as 0.83 (Fig. 10b). In the entire volume scan, the maximum radar reflectivity

factor was 71 dBZ at ~ 4.6 km ARL. The freezing level was ~ 3.1 km ARL, and the melting layer extended down to ~ 1.9 km ARL. Thus, the TBSS at 0.5° -elevation angle was below the freezing level.

In this example, a few TBSS radar gates are misclassified as BS in the HCA output (Fig. 10d). As in the first example, the misclassifications are nonmeteorological, which has no effect on the quality-controlled radar reflectivity factor (Fig. 10c). Otherwise, there are no obvious false TBSS gates present in the HCA output for this storm.

The fourth event the modified HCA is tested on occurred on 29 March 2013. Radar data collected by the KTLX WSR-88D near Norman, Oklahoma, are used. In this event, an evening thunderstorm produced a 6.4-cm-diameter hailstone at the surface at approximately 2342 UTC. Figure 11 presents the radar scan from the 1.3° -elevation angle at 2341 UTC, approximately a minute

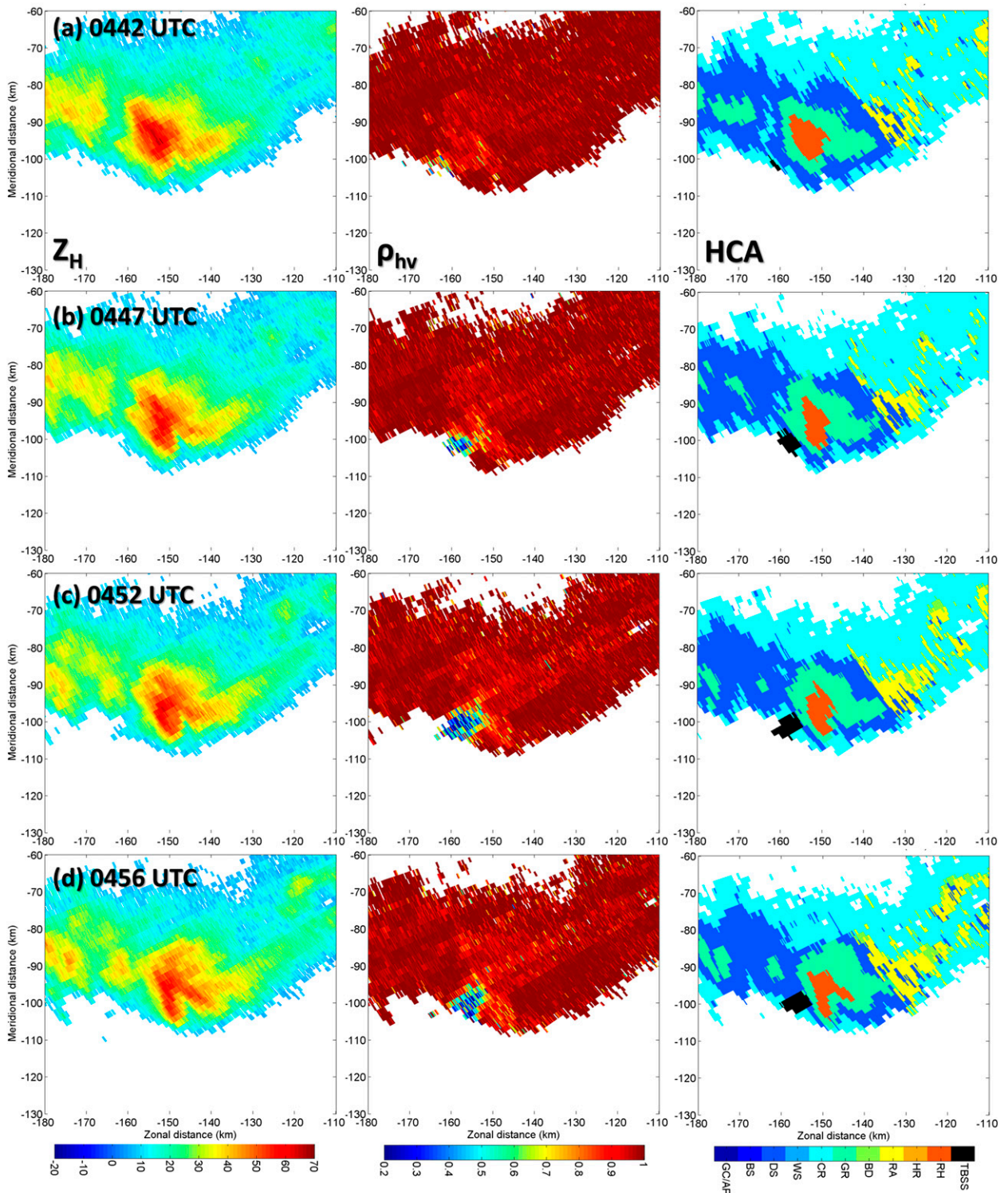


FIG. 8. Example event on 30 Mar 2012 from KVNx that shows the time evolution of a developing TBSS at 0.5°-elevation angle. Shown are (left) Z_H , (center) ρ_{hv} , and (right) enhanced hydrometeor classification at (a) 0442, (b) 0447, (c) 0452, and (d) 0456 UTC.

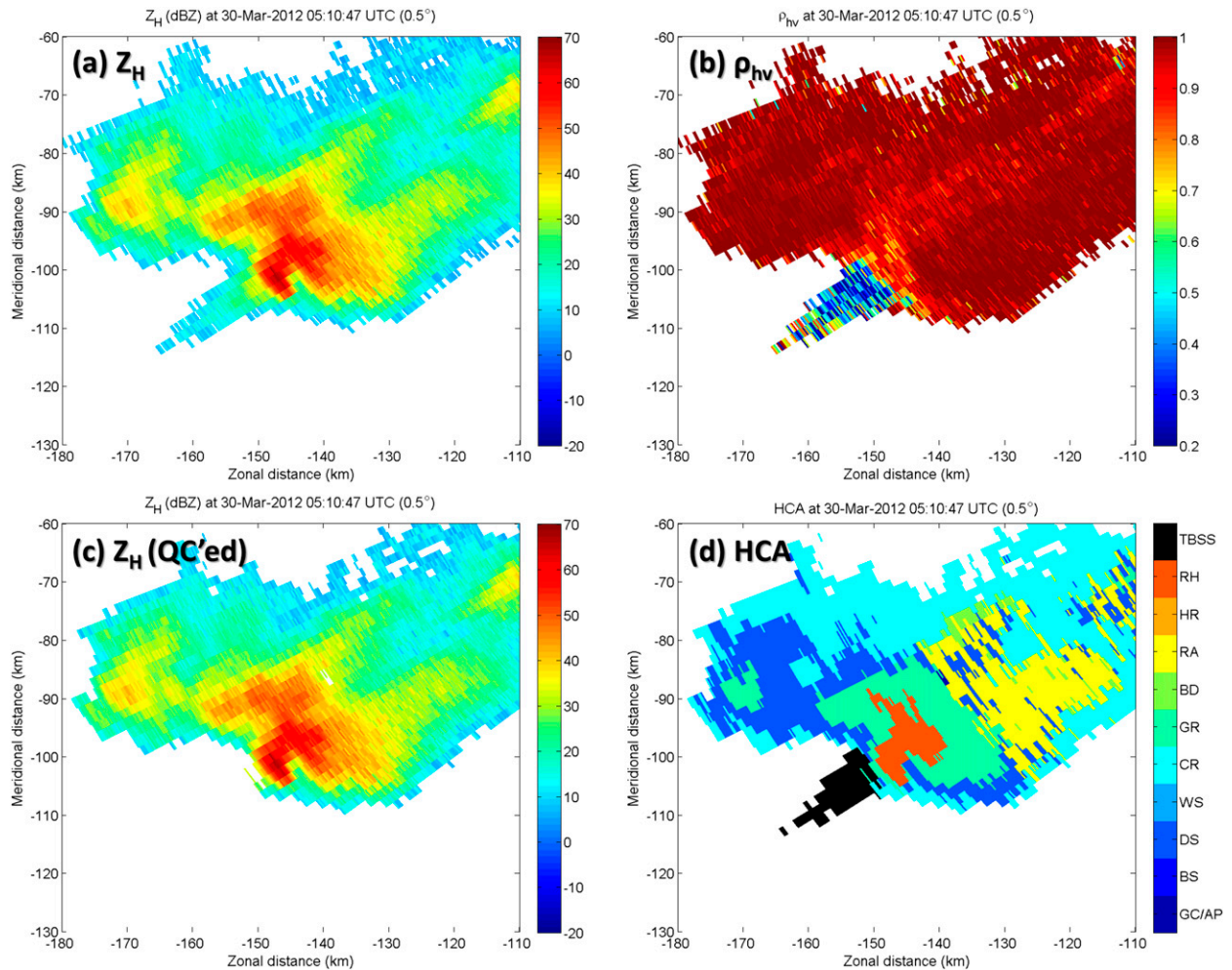


FIG. 9. As in Fig. 7, but for an example event on 30 Mar 2012 from KVNx associated with 10.2-cm hail at the surface.

before the hailstone was reported at the surface. At the 1.3° -elevation angle, the maximum radar reflectivity factor is 69.5 dBZ at ~ 1.7 km ARL (Fig. 11a). The ρ_{hv} within the 69.5-dBZ gate is 0.94; however, an adjacent radar gate has ρ_{hv} as low as 0.62 (Fig. 11b). Several other radar gates with ≥ 60 dBZ have $\rho_{hv} < 0.80$, indicating the presence of hail. Within the entire volume scan, the maximum radar reflectivity factor was 72 dBZ at ~ 2.2 km ARL. The freezing level was ~ 2.8 km ARL, and the melting layer extended down to ~ 1.8 km ARL. Therefore, the TBSS at 1.29° -elevation angle was below the freezing level, but within the approximate melting layer.

In this case, a few TBSS radar gates are misclassified as CR; however, the underdetection of TBSS generally seems limited (Fig. 11d). There is a sharp cutoff of reflectivity in the quality-controlled radar reflectivity factor (Fig. 11c), which is associated with a sharp gradient in ρ_{hv} where the HCA transitions from RH or RA to

TBSS class. For example, on one of the azimuths, ρ_{hv} decreases radially from 0.98 to 0.44 in one radar gate. As in the second event, it is reasonable to assume that within some of the TBSS class immediately downrange from the RH or RA class there is a mix of radar returns from both the TBSS artifact and hydrometeors. This demonstrates a significant downside of this HCA; it only outputs the highest aggregation and does not take into account the possibility that a sampling volume may have multiple classes except in the case of RH. In those radar gates, it is possible both hydrometeors and TBSS contribute to the reflectivity. However, the radar echoes are dominated by TBSS, which has a larger contribution to the reflectivity than the hydrometeors.

The final event the HCA is tested on occurred on 22 April 2013 near KICT, the Wichita, Kansas, WSR-88D. In this event, an evening supercell produced a 5.1-cm-diameter hailstone at the surface at approximately 0004 UTC 23 April 2013. Figure 12 is the radar scan from

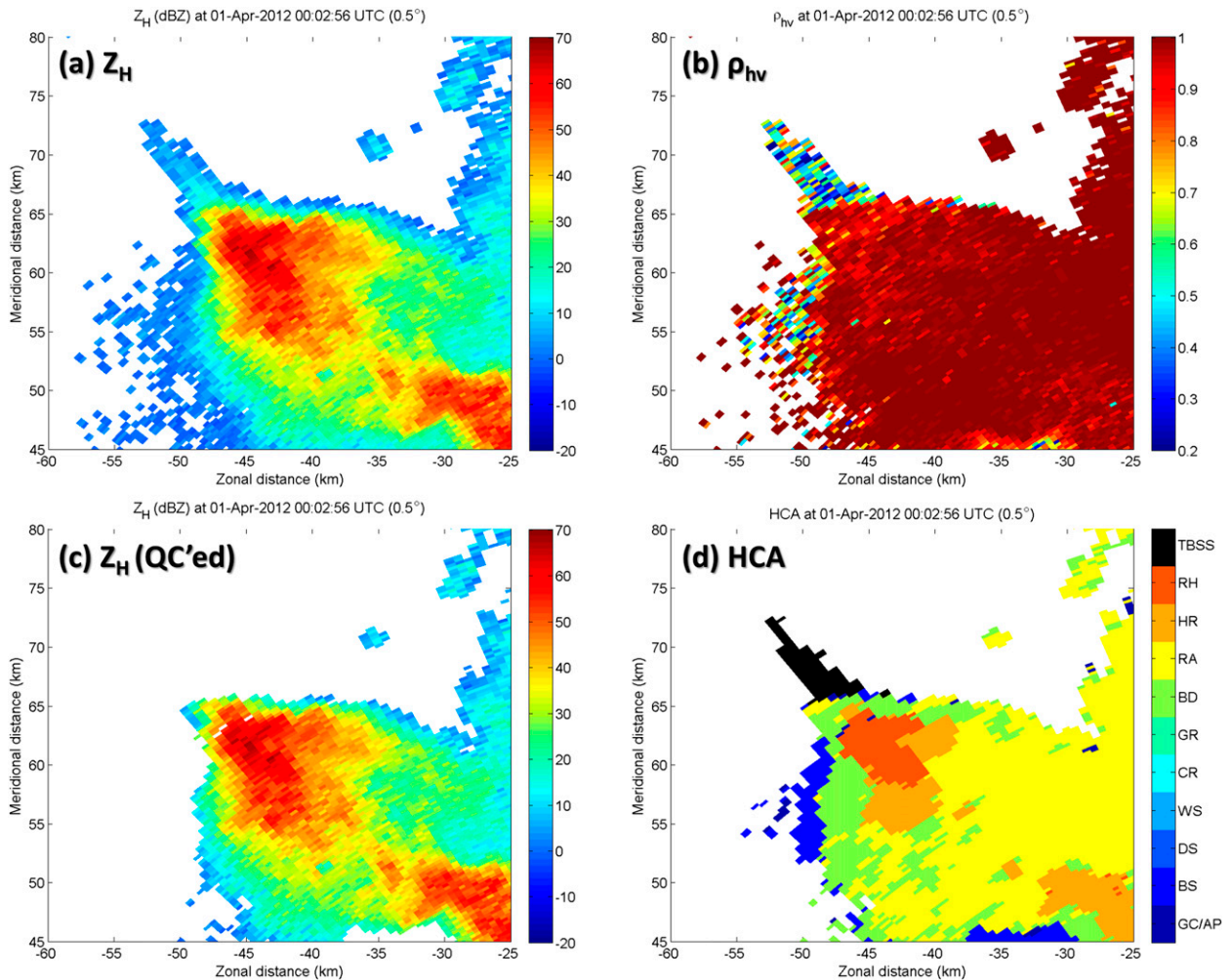


FIG. 10. As in Fig. 7, but for an example event on 1 Apr 2012 from KBMX associated with 7.6-cm hail at the surface.

the 1.3°-elevation angle at 2359 UTC, approximately 5 min before the hailstone was reported at the surface. At the 0.5°-elevation angle, the maximum radar reflectivity factor is 74 dBZ at ~ 2.2 km ARL (Fig. 12a). This was also the maximum within the entire volume of the storm. The ρ_{hv} is reduced to < 0.80 for several gates within the hail core (Fig. 12b). In some gates, it is anomalously low (< 0.70) within high reflectivity (≥ 60 dBZ). The freezing level was ~ 2.9 km ARL, and the melting layer extended down to ~ 1.8 km ARL. As a result, the TBSS at 0.5°-elevation angle was below the freezing level, but within the approximate melting layer.

In the HCA output, there is possible overidentification of TBSS on the southern part of the storm (Fig. 12d). As a result, a nearly enclosed hole is present on the southern part of the storm in the quality-controlled radar reflectivity factor (Fig. 12c). Once again, there is a sharp gradient in reflectivity. A decrease of ρ_{hv} within this region is probably the reason for the slight overidentification of

TBSS. The reduced ρ_{hv} could possibly be because of nonuniform beam filling or low SNR. Outside of this region, the identification of TBSS seems quite reasonable.

4. Summary and conclusions

The three-body scatter signature, or TBSS, is a radar artifact that appears downrange from a high-reflectivity core in a thunderstorm. Previous studies have shown that TBSSs have been precursors to severe weather such as large hailstones and damaging winds at the surface. Therefore, identification of TBSS is useful for severe-weather operations. Since TBSS is a radar artifact, identification and removal are also important for the quality control of radar data used in NWP and QPE. In this paper, an automated method for identifying TBSS in S-band radar data was developed for possible real-time applications.

The current S-band WSR-88D network that is in operational use in the United States uses a version of the

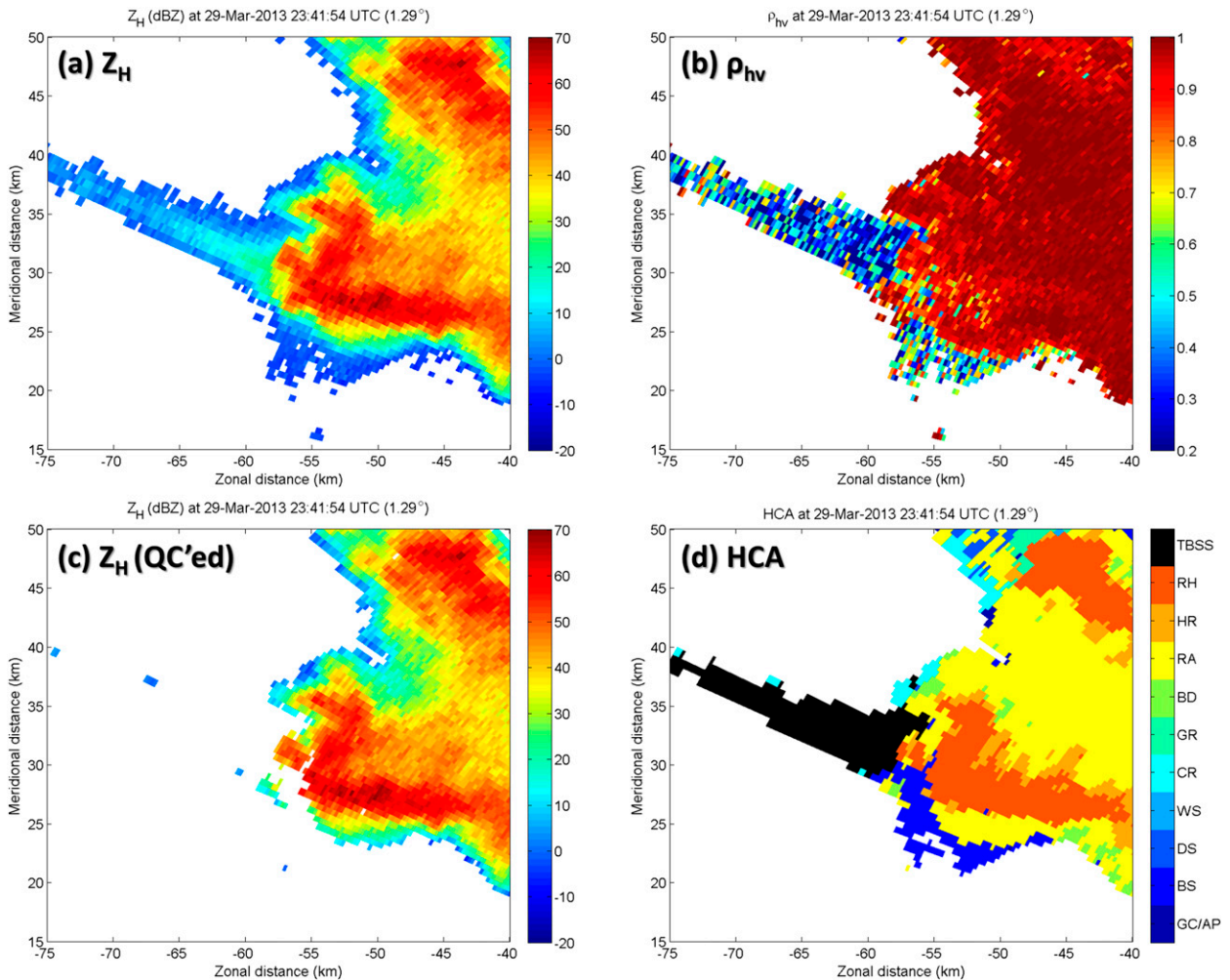


FIG. 11. As in Fig. 7, but for an example event on 29 Mar 2013 from KTLX associated with 6.4-cm hail at the surface.

P09 HCA to distinguish among 10 classes of hydrometeors for level-3 data products. TBSS was added as a new 11th class. Using true polarimetric radar measurements, trapezoidal membership functions were developed using statistics of data that were manually selected. These membership functions allowed for the addition of a TBSS class to an enhanced HCA based upon the P09 HCA for S-band radars.

The results of the TBSS classification are promising, as indicated by the rather reliable identification of TBSSs in five significant hail events tested. The identifications were not perfect though. There were examples of possible over- and underidentification of the TBSS class. In the overidentification cases, the quality-controlled reflectivity factor had a sharp cutoff of reflectivity. These radar gates tended to have a sharp radial decrease in ρ_{hv} . Therefore, it is reasonable to assume there was a mix of radar returns from both the TBSS artifact and the hydrometeors within these radar gates. The membership functions and weights

were determined using a dataset that appeared to be pure TBSS (or at least the TBSS is the dominant signal), so mixtures may result in quality-control errors where TBSS is not the dominant signal. Overidentification is also possible in areas of low SNR because of reduced ρ_{hv} , and large errors in Z_{DR} and Φ_{DP} . The underidentification cases occurred when the TBSS was below the melting layer. Generally, the TBSS was misclassified as biological scatterers. For the quality-controlled radar reflectivity factor, this misclassification has no effect on the results because all nonmeteorological targets are removed. Note that all misclassifications are speculative because the truth is not completely known. Even with the possible misclassifications, the results are promising enough that the new TBSS membership functions could be eventually implemented operationally. The algorithm can be further tuned by testing it on a much larger number of hail cases before such operational implementation. Similar algorithms can also be developed for radars at

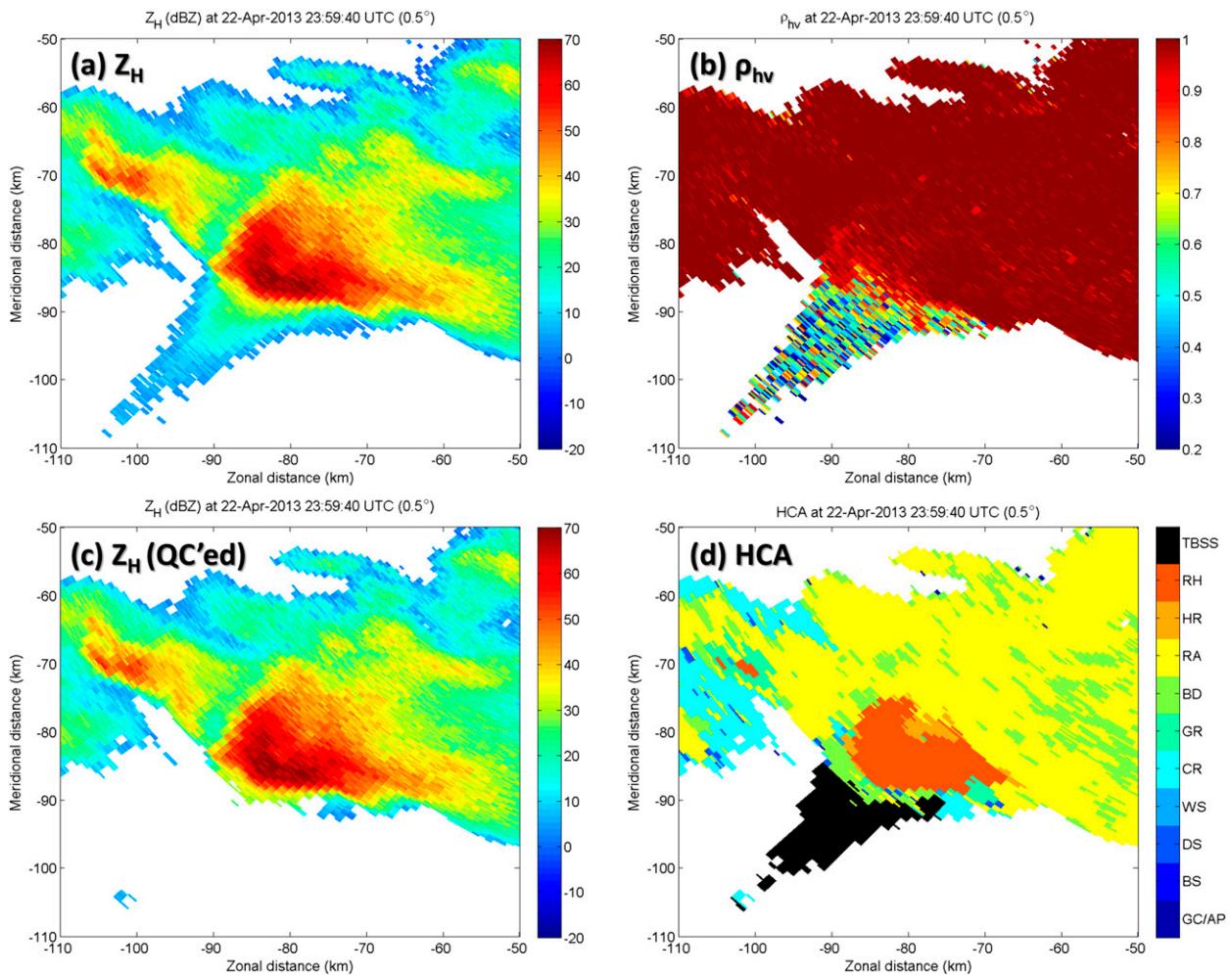


FIG. 12. As in Fig. 7, but for an example event on 22 Apr 2013 from KICT associated with 5.1-cm hail at the surface.

other wavelengths, such as X- and C-band radars, where attenuation and other factors will play a role. These developments are planned for the future.

Acknowledgments. The authors thank John Krause at the Cooperative Institute for Mesoscale Meteorological Studies (CIMMS) for providing code to convert raw WSR-88D data to netCDF format. This work was supported by NSF Grant AGS-1046171. The third author was also supported by NSF Grant AGS-0802888.

REFERENCES

- Bohren, C. F., and D. R. Huffman, 1983: *Absorption and Scattering of Light by Small Particles*. John Wiley and Sons, 530 pp.
- Hubbert, J. C., and V. N. Bringi, 2000: The effects of three-body scattering on differential reflectivity signatures. *J. Atmos. Oceanic Technol.*, **17**, 51–61, doi:10.1175/1520-0426(2000)017<0051:TEOTBS>2.0.CO;2.
- Kumjian, M., J. Picca, S. Ganson, A. Ryzhkov, and D. Zrnić, 2010: Three-body scattering signatures in polarimetric radar data. NOAA/NSSL Rep., 12 pp. [Available online at https://www.nssl.noaa.gov/publications/wsr88d_reports/FINAL_TBSS.doc.]
- Lemon, L. R., 1998: The radar “three-body scatter spike”: An operational large-hail signature. *Wea. Forecasting*, **13**, 327–340, doi:10.1175/1520-0434(1998)013<0327:TRTBSS>2.0.CO;2.
- Lim, S., V. Chandrasekar, and V. N. Bringi, 2005: Hydrometeor classification system using dual-polarization radar measurements: Model improvements and in situ verification. *IEEE Trans. Geosci. Remote Sens.*, **43**, 792–801, doi:10.1109/TGRS.2004.843077.
- Lindley, T. T., and L. R. Lemon, 2007: Preliminary observations of weak three-body scattering spikes associated with low-end severe hail. *Electron. J. Severe Storms Meteor.*, **2** (3). [Available online at <http://www.ejssm.org/ojs/index.php/ejssm/article/viewArticle/12/22>.]
- Liu, H., and V. Chandrasekar, 2000: Classification of hydrometeors based on polarimetric radar measurements: Development of fuzzy logic and neuro-fuzzy systems, and in situ verification. *J. Atmos. Oceanic Technol.*, **17**, 140–164, doi:10.1175/1520-0426(2000)017<0140:COHBOP>2.0.CO;2.
- Marzano, F. S., D. Scaranari, M. Celano, P. P. Alberoni, G. Vulpiani, and M. Montopoli, 2006: Hydrometeor classification from dual polarized weather radar: Extending fuzzy logic from S-band to C-band. *Adv. Geosci.*, **7**, 109–114, doi:10.5194/adgeo-7-109-2006.

- Office of the Federal Coordinator for Meteorological Services and Supporting Research, 2013: Doppler radar meteorological observations. Part A—System concepts responsibilities and procedures. *Federal Meteorological Handbook No. 11*, Office of the Federal Coordinator for Meteorological Services and Supporting Research. [Available online at <https://ams.confex.com/ams/pdfpapers/88063.pdf>.]
- Oye, R., C. Mueller, and S. Smith, 1995: Software for radar translation, visualization, editing, and interpolation. Preprints, *27th Conf. on Radar Meteorology*, Vail, CO, Amer. Meteor. Soc., 359–361.
- Park, H. S., A. V. Ryzhkov, D. S. Zrnić, and K.-E. Kim, 2009: The hydrometeor classification algorithm for the polarimetric WSR-88D: Description and application to an MCS. *Wea. Forecasting*, **24**, 730–748, doi:10.1175/2008WAF2222205.1.
- Picca, J., and A. Ryzhkov, 2012: A dual-wavelength polarimetric analysis of the 16 May 2010 Oklahoma City extreme hailstorm. *Mon. Wea. Rev.*, **140**, 1385–1403, doi:10.1175/MWR-D-11-00112.1.
- Ryzhkov, A. V., T. J. Schuur, D. W. Burgess, and D. S. Zrnić, 2005: Polarimetric tornado detection. *J. Appl. Meteor.*, **44**, 557–570, doi:10.1175/JAM2235.1.
- Schuur, T. J., A. V. Ryzhkov, and P. L. Heinselman, 2003: Observations and classification of echoes with the polarimetric WSR-88D radar. NOAA/National Severe Storms Laboratory Rep., 46 pp.
- Snyder, J. C., H. B. Bluestein, G. Zhang, and S. J. Frasier, 2010: Attenuation correction and hydrometeor classification of high-resolution, X-band, dual-polarized mobile radar measurements in severe convective storms. *J. Atmos. Oceanic Technol.*, **27**, 1979–2001, doi:10.1175/2010JTECHA1356.1.
- SPC, cited 2013: Storm reports. Storm Prediction Center. [Available online at <http://www.spc.noaa.gov/climo/>.]
- Straka, J. M., and D. S. Zrnić, 1993: An algorithm to deduce hydrometeor types and contents from multiparameter radar data. Preprints, *26th Conf. on Radar Meteorology*, Norman, OK, Amer. Meteor. Soc., 513–516.
- Vivekanandan, J., D. S. Zrnić, S. Ellis, D. Oye, A. V. Ryzhkov, and J. M. Straka, 1999: Cloud microphysics retrieval using S-band dual-polarization radar measurements. *Bull. Amer. Meteor. Soc.*, **80**, 381–388, doi:10.1175/1520-0477(1999)080<0381:CMRUSB>2.0.CO;2.
- Wilson, J. W., and D. Reum, 1986: “The hail spike”: Reflectivity and velocity signature. Preprints, *23rd Conf. on Radar Meteorology*, Snowmass, CO, Amer. Meteor. Soc., 62–65.
- , and —, 1988: The flare echo: Reflectivity and velocity signature. *J. Atmos. Oceanic Technol.*, **5**, 197–205, doi:10.1175/1520-0426(1988)005<0197:TFERAV>2.0.CO;2.
- Zrnić, D. S., 1987: Three-body scattering produces precipitation signature of special diagnostic value. *Radio Sci.*, **22**, 76–86, doi:10.1029/RS022i001p00076.
- , and A. V. Ryzhkov, 1999: Polarimetry for weather surveillance radars. *Bull. Amer. Meteor. Soc.*, **80**, 389–406, doi:10.1175/1520-0477(1999)080<0389:PFWSR>2.0.CO;2.
- , —, J. M. Straka, Y. Liu, and J. Vivekanandan, 2001: Testing a procedure for the automatic classification of hydrometeor types. *J. Atmos. Oceanic Technol.*, **18**, 892–913, doi:10.1175/1520-0426(2001)018<0892:TAPFAC>2.0.CO;2.